Reflective low-sideband plasmonic structural colors

Jun Zheng[1,2], Zhi-Cheng Ye[3,4*], Zheng-Ming Sheng[1,2,5]

[1]*Key Laboratory for Laser Plasmas (Ministry of Education) and Department of Physics and astronomy, Shanghai Jiao Tong University, Shanghai, 200240, China*

[2] *Collaborative Innovation Center of IFSA (CICIFSA), Shanghai Jiao Tong University, Shanghai, 200240, China*

[3]*National Engineering Laboratory for TFT-LCD Technology, Department of Electronic Engineer, Shanghai Jiao Tong University, Shanghai, 200240, China*

[4]*State Key Laboratory on Integrated Optoelectronics, Institute of Semiconductors, Chinese Academy of Sciences, Beijing 100083, China*

[5]*SUPA and Department of Physics, University of Strathclyde, Glasgow G4 0NG, UK*

[*] yzhch@sjtu.edu.cn

Abstract: It is demonstrated experimentally that an aluminum (Al) nanowire grating structure on silicon substrates can produce low-side-band monochromatic peak when it reflects colored light in the transverse magnetic (TM) mode. The central wavelength of the reflection is shown to be sensitive to the incident angle, which leads to significant color shifts. Formation of the monochromatic peak is attributed to the surface plasmon resonance on the interface between Al and air, together with remarkable diffraction at shorter wavelengths and strong Fabry-Perot (F-P) resonance absorption by Al-surrounding nano-cavities and silicon substrate at longer wavelengths. In contrast, reflection in transverse electric (TE) mode does not show distinct wavelength selectivity due to the cut-off effect of the nano-cavities. The outstanding characters of the proposed structure with polarization dependence, high sensitivity to incident angle, high color rendering facilitate more compact and sophisticated color-filter-based devices for displays, anti-counterfeit, and sensing applications. In addition, the two-dimensional structure with thin grating thickness and high duty ratio tolerance is relatively easy for fabrication.

OCIS codes: (240.6680) Surface plasmons; (230.1950) Diffraction gratings; (050.6624) Subwavelength structures; (230.5440) Polarization-selective devices

References and links

1. V. Finlay, *Color: A Natural History of the Palette*, (Random House, 2004).
2. P. Vukusic and J. R. Sambles, "Photonic structures in biology," Nature **424**, 852 (2003).
3. R. Magnusson and S. S. Wang, "New principle for optical filters," Appl. Phys. Lett. **61**, 1022 (1992).
4. Y. Kanamori, M. Shimono, and K. Hane, "Fabrication of transmission color filters using Silicon subwavelength gratings on quartz substrates," IEEE Photonics Tech. Lett. **18**, 2126 (2006).
5. E. Cho, H. Kim, B. Cheong, P. Oleg, W. Xianyuan, J. Sohn, D. Ma, H. Choi, N. Park, and Y. Park, "Two-dimensional photonic crystal color filter development," Opt. Express **17**, 8621 (2009).
6. C. Genet and T. W. Ebbesen, "Light in tiny holes," Nature **445**, 39 (2007).
7. H. Liu and P. Lalanne, "Microscopic theory of the extraordinary optical transmission," Nature **452**, 728 (2008).
8. Q. Chen and D. Cumming, "High transmission and low color cross-talk plasmonic color filters using triangular-lattice hole arrays in aluminum films," Opt. Express **18**, 14056 (2010).
9. D. Franklin, Y. Chen, A. Vazquez-Guardado, S. Modak, J. Boroumand, D. Xu, S. Wu, and D. Chanda, "Polarization-independent actively tunable colour generation on imprinted plasmonic surfaces," Nat. Commun. **6**, 7337 (2015).
10. H. S. Lee, Y. T. Yoon, S. S. Lee, S. H. Kim, K. D. Lee, "Color filter based on a subwavelength patterned metal grating," Opt. Express **15**, 15457 (2007).
11. T. Ellenbogen, K. Seo, and K. Brozier, "Chromatic plasmonic polarizers for active visible color filtering and polarimetry," Nano Lett. **12**, 1026 (2012).
12. H. Lezec, A. Degiron, E. Devaus, R. Linke, L. Martin-Moreno, F. Garcia-Vidal, T. Ebbesen, "Beaming light from a subwavelength aperture," Science **297**, 820 (2002).
13. Y. Wu, A. Hollowell, C. Zhang, and L. Guo, "Angle-insensitive structural colours based on metallic nanocavities and coloured pixels beyond the diffraction limit," Sci. Rep. **3**, 1194 (2013).

14. J. Zheng, Z.C. Ye, N.L. Sun, R. Zhang, Z.M. Sheng, H.P. Shieh, J. Zhang, "Highly anisotropic metasurface: a polarized beam splitter and hologram," Sci. Rep. **4**, 649 (2014).
15. P. Albella, B. Garcia-Cueto, F. González, F. Moreno, P. C Wu, T. H. Kim, A. Brown, Y. Yang, H. O. Everitt, and G. Videen, "Shape Matters: Plasmonic Nanoparticle Shape Enhances Interaction with Dielectric Substrate," Nano Lett. **11**, 3531 (2011).
16. B. Baloukas , W. Trottier-Lapointe, L. Martinu,, "Fabry-Perot-like interference security image structures: From passive to active," Thin Solid Films **559**, 9 (2014).
17. S Kinoshita, S Yoshioka and J Miyazaki , "Physics of structural colors," Rep. Prog. Phys. **71**, 076401 (2008).
18. A. Rakić, A. Djuriš ić, J. Elazar, L. Marian, and M. Majewski, "Optical properties of metallic films for vertical-cavity optoelectronic devices," Appl. Opt. **37**, 5271(1998).

1. Introduction

Color filters are key components in display devices, image sensors, optical communications, and especially in the anti-counterfeit tags. Generally, there are two approaches to make colored pictures, i.e. using absorptive pigments [1] or optical structures [2]. The pigments can selectively absorb certain wavelengths of incident light and let other wavelengths be reflected or transmitted. While structural colors rely on the light interference and diffraction from the periodic micro-nano structures or lamellar films with alternate refractive indexes. Owing to the rapidly development of nano-fabrication technology, considerable attention has been paid to the artificial subwavelength structures which can generate peculiar spectra not available in the natural world. Compared with the pigment color filters, structure-based color filters like dielectric photonic crystals [3-5] and metallic nano-arrays [6-11] can increase the optical systems' light efficiency due to the non-absorptive physical mechanism therein and their thin film character, making it possible to produce more compact device. Moreover, they can be integrated with polarization feature [11]. The physical mechanisms in these structural colors mainly include guided-mode resonance (GMR) of planar dielectric waveguide grating and surface plasmon resonance (SPR) of metallic surface [12]. Plasmonic nanostructures are promising to efficiently control light via the conversion between photons and plasmons at subwavelength scale, which may provide new solutions to traditional optical processes such as color filter, spectral imaging, and active electro-optic control. Studies show that the metallic gratings [13-14] are the favorable candidates for a variety of applications, not only due to their compact structures, excellent spectral characteristics and simple fabrication process, but also for the close dependence of the resonant wavelength on the incident light angle and polarization via SPR [15].

Based on a subwavelength metal nanowire grating (MNG) on silicon substrates, we report a polarization-dependent and reflection-type plasmonic structure color device, which produces a narrow band reflection with transverse magnetic (TM, electric field perpendicular to the grating stripes) field and broad band reflection with transverse electric (TE, electric field parallel to the grating stripes) field, displaying distinct difference in color. Monochromatic-peaks across the entire visible light are persistent and obtained easily by changing the incident angle of the input white light. With this unique optical function, the proposed MNGs can be used to engineer visible light color in displays, polarization microscopy, polarimetry, and especially in encrypted tags for security applications which has a more judgment of color in reflection, besides the diffraction effect used in conventional grating based tags. This bi-layer metallic grating structure, the thin grating thickness and high duty ratio tolerance make the proposed plasmonic structural color device easy to fabricate.

2. Plasmonic Structural Colors

Figure 1(a) presents the schematic diagram of the proposed reflected plasmonic structure color device, where the chromatic beam splitting of reflection, diffraction and absorption for an incident unpolarized white light is illustrated as well. The lateral SPR induced TM reflection peak with wavelength λ_{SPR} is presented with a green arrow. The TM light with the wavelength shorter than λ_{SPR} is diffracted mainly and with the wavelength longer than λ_{SPR} is absorbed by the nano-cavities embedded in the structures and the silicon substrate which are

presented by red oval shapes marked by 'A_{cavity}' and '$A_{substrate}$', respectively. The TE incident white light is mainly reflected. Scanning electron microscopy (SEM) images of the top and side views of the fabricated device in Fig. 1(b) clearly show a layer of Al film conformally deposited on dielectric reliefs. In the fabrication process, a poly-methyl-methacrylate (PMMA) grating with pitch T=420 nm, slit width w=210 nm, i.e. duty cycle w/T of 50% and reliefs height h_1=90 nm was fabricated by nano-imprinting on the silicon wafers. Then, the grating was deposited with an aluminum (Al) film of thickness h_2=40 nm by electron beam (E-beam) evaporation. In addition to the two layers of Al formed on the top of the PMMA ridges and in the grooves, the sidewalls of the PMMA bars were also coated with Al with width of about 5 nm.

In the measurement, a collimated white light was polarized by a Glen-Thompson prism and then was illuminated on the device fixed on a motor-driven rotating stage. The reflected light was collected by a fiber mounted with a collimating lens connected to a spectrometer (QE65-PRO, Ocean Optics).

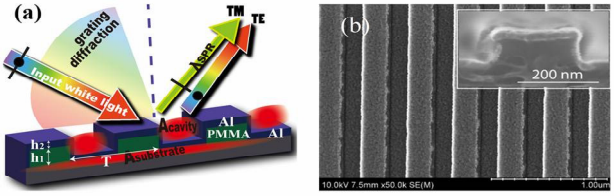

Fig. 1. (a) The schematic diagram of the reflective plasmonic structure color device. (b) SEM images of the top and side views of a fabricated device. The PMMA grating pitch is T=420 nm with duty cycle of 50%, the thickness of the dielectric and aluminum are h_1 = 90 nm and h_2 =40 nm, respectively, the sidewalls of the PMMA bars are coated with Al with width of about 5 nm.

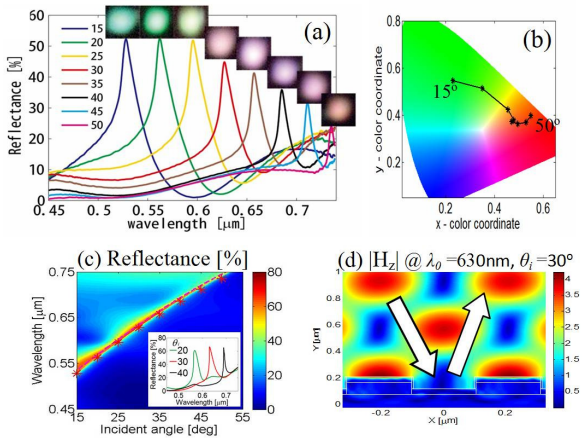

Fig. 2. (a) Measured reflected spectra and the corresponding color patterns for the incident TM white light with incident angles from 15° to 50°. (b) The locations of measured reflected spectra in the CIE 1931 xy chromaticity diagram. (c) The simulated reflection spectra for different incident angles. The magenta dashed line and the red stars represent the calculated λ_{SPR} and the measured reflected peaks, respectively. The inset shows the reflection spectra for θ_i= 20°, 30° and 40°. (d) The steady amplitude distribution of the simulated magnetic field H_z for an incident TM light with wavelength of 630 nm and incident angle of 30°. The incident and reflected light are depicted by the white arrows, respectively. The white lines schematically depict the profile of the structure. The amplitude of the incident magnetic field is 1.0. The parameters used in this simulation is the same as that of the fabricated device shown in Fig. 1.

2.1 TM reflection with a single peak

The measured TM reflected spectra for the incident angles θ_i from 15° to 50° are presented in Fig. 2(a), where a series of distinct peaks corresponding to the different incident angles with high reflectance at λ_{SPR} and low reflectance at other wavelengths are shown. Generally, the

maximum reflected efficiencies are more than 32% and the full width at half maximum is only about 28 nm which is narrower than that of the Fabry-Perot-like interference multilayered structures for security image with typical value of 50 nm [16, 17], especially when θ_i is less than 25° as high as 52% reflection can be obtained. The measured reflected color patterns are also presented on top of corresponding spectra. The reflected spectra's corresponding locations in the CIE 1931 xy chromaticity diagram are presented in Fig. 2(b), which shows that the color is changed from green to yellow and then to red with the increase of incident angle. The sharp reflection peak at λ_{SPR} corresponds to the lateral SPR, which is described by the equation $k_0 \sin\theta_i + mG = k_{SPP}$ (m = 0, ±1, ±2, …) with negative first-order of reciprocal vector of the modulation (m = -1), where, k0 is the wave number of the light in vacuum; the grating vector $G = 2\pi/T$; the wave number of the surface plasma polariton, ε_0 and ε_m are the permittivity of the air and Al by Lorantz-Drude mode [18] respectively. The calculated resonant wavelengths λ_{SPR} under different incident angles are shown as magenta dashed line in the simulated reflected spectra by rigorous coupling wave analysis (Diffraction Mode, RSOFT) in Fig. 2(c), where the measured reflected peaks are also shown as red stars. These experimental, analytical and simulated results are coincident very well. The steady amplitude distribution of the simulated magnetic field Hz for incident TM light with wavelength of 630 nm and incident angle of 30° is shown in Fig. 2(d) to represent the reflection straightforward. It is clear that the light almost does not enter into the air cavities and is directly reflected at the surface of the top aluminum via the SPR enhancement and light interference effect between the incident and the reflected lights.

2.2 TE reflection with wide spectrum brand

Different from the TM case, the measured and simulated TE reflection spectra show wide-band character with most of the light being reflected as shown in Fig. 3(a) and 3(b). The steady amplitude distribution of the simulated electric field Ez in Fig. 3(c) shows that the incident TE light with wavelength of 630 nm cannot enter the air cavities due to the absence of plasmonic waveguide mechanism and such that, is directly reflected.

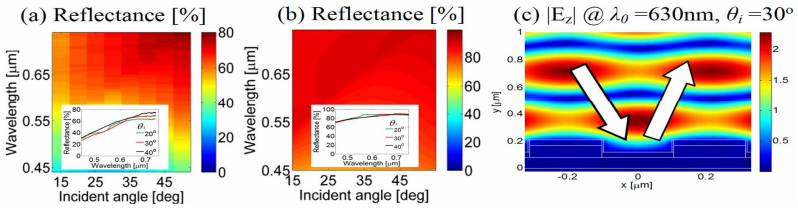

Fig. 3. (a) Measured reflection spectra for the TE white light with incident angles from 15° to 50°. (b) The simulated reflection spectra. The insets in (a-b) show the reflection spectra for θ_i= 20°, 30° and 40°. (c) The steady amplitude distribution of the simulated electric field E_z for an incident light with wavelength of 630 nm and incident angle of 30°. The incident and reflected light are depicted by the white arrows, respectively. The white lines schematically depict the profile of the device structure. The amplitude of the incident electric field is 1.0. The structure used in this simulation is the same as that of the fabricated device shown in Fig. 1.

3. Discussion

To analyze the sharp-peaked character of TM reflection, we divide the reflection spectra into three zones: diffraction, SPR and absorption zone beyond diffraction effect. The simulated -1st order diffraction spectra is displayed in Fig. 4(a), which manifests that more than 60% of the incident TM light energy with wavelength $\lambda < \lambda_{SPR}$ is diffracted. The measured diffraction patterns from the device for the incident TM white light with incident angles of 25° and 50° are also presented therein. The maximum wavelengths λ_{Diff} of the -1st order diffraction is shown as magenta dashed lines in Fig. 4(a) and 4(b), which is deduced from diffraction equation $k_0 \sin\theta_i + mG = k_0 \sin\theta_D$ (m = ±1, ±2, …) with the diffraction angle θ_D= 90°. The diffraction limit λ_{Diff} is a few nanometers shorter than λ_{SPR}, so the light with wavelength of λ_{SPR} cannot be diffracted. The steady amplitude distribution of the simulated H_z for λ_0= 530 nm and

θ_i =30° in Fig. 4(c) represents the diffraction process: the light enters the air cavities in surface plasmon waveguide mode [14] and then is diffracted straight forward.

Further simulation of absorption in Fig. 4(b) shows that more than 70% of the incident energy of light with $\lambda > \lambda_{SPR}$ is absorbed. The simulated stable amplitude distribution of Hz in Fig. 4(d) shows that these incident lights are mostly trapped and absorbed in the Al-surrounding cavities via Fabry-Perot (F-P) destructive reflection interference [13] and silicon substrate via SPR. The cavity's parameters' effects are analyzed thoroughly in the following.

In short, by the combination of the above three mechanisms: SPR enhanced reflection, grating diffraction of the shorter wavelengths and plasmonic waveguide enhanced F-P resonant absorption of the longer wavelengths, the reflective TM sharp peak is obtained.

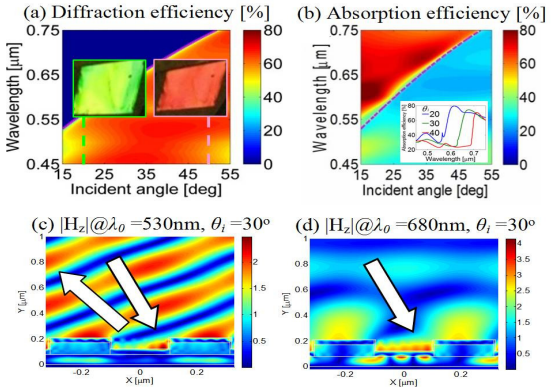

Fig. 4. (a-b) The simulated diffraction spectra (a) and absorption spectra (b) for the different incident angles. The magenta dashed lines represent the diffraction limited wavelength λ_{Diff}. The insets in (a) represent the measured diffraction patterns for the incident TM white light with incident angle of 25° and 50°. The inset in (b) shows the absorption spectra for θ_i= 20°, 30° and 40°. (c-d) The steady amplitude distribution of the simulated magnetic field H_z for a wavelength of 530 nm (c) and 680 nm (d) and incident angle of 30°, respectively. The incident and diffracted light are depicted by the white arrows, respectively. The white lines schematically depict the profile of the device structure. The amplitude of the incident magnetic field is 1.0. The structure used in this simulation is the same as that of the fabricated device shown in Fig. 1.

To present a comprehensive picture of the three correlative mechanisms of diffraction, SPR, and F-P resonance, the simulated efficiencies of diffraction, reflection and absorption with the change of depth and width of the air cavities and the pitch of the grating are shown in Fig. 5 and 6, respectively. The optical efficiencies for every wavelength behave as alternative bright and dark bands with the change of cavity depth h_1, which can be described by the phase difference $4\pi n_{eff} h_1/\lambda$ between lights reflected by the metal on the top of the grating and on the bottom of the cavities, where n_{eff} is the effective refractive index in the cavities. As shown in Fig. 5(b), the mono-peaked reflection with low side band character can be obtained for 120 nm>h_1>60 nm and 350 nm>h_1>300 nm, where h_1 smaller than 100 nm is preferable for more convenient fabrication. Figure 5 also show that the modulation of TM light is obviously much stronger than that of TE light, which further confirms that TM light can propagate in the slits via metal-insulator-metal waveguide mode efficiently, thus have stronger F-P cavity resonance. While, for TE light, the longer the wavelength is, the more obvious the prohibition effect of the slit to the light is, thus only shorter wavelength light can enter the slits in waveguide mode and has periodical effect with the cavity thickness, as shown in Fig. 5(d-f). Even with F-P enhancement effect, the maximum diffraction efficiency of TE light diffraction efficiency can only reach 45% for h_1 =210 nm and wavelengths smaller than 500 nm.

Beside the height of cavities, the effective refractive index of the cavity also affects the F-P resonance. However, as shown in Fig. 6(a), by changing the duty cycle from 0.3-0.6, i.e. decreasing n_{eff}, the peak-shaped reflection is mainly kept due to the fact that the center

wavelength of the reflected peak is determined by SPR related to incident angle mentioned above and grating pitch. In Fig. 6(b), the fine engineering of the reflected wavelengths by the grating pitch from 350 nm to 490 nm is shown, which is corresponding to the obvious shift of colors from green to red as presented in Fig. 6(c). Thus, in the real application, by choosing pitch and controlling the width and height of the cavity in an appropriate range, one can obtain desired reflected plasmonic structure color based on the MNGs with mono peak and low side band. It is noticed that the TE reflection behaves wide band character. The giant different colors between TM and TE lights in this device, which can be readily observed using a cheap Polyvinyl alcohol film polarizers, make it to be easily discriminated from conventional unpolarized diffractive holograms commonly used in security tags.

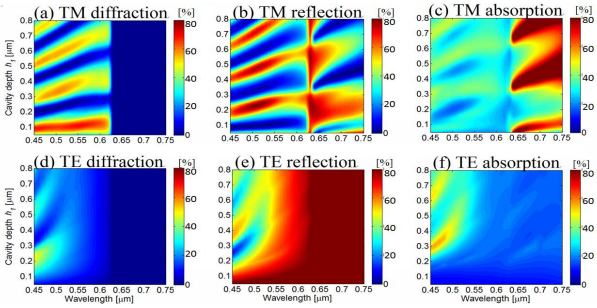

Fig. 5. The simulated diffraction (a, d), reflection (b, e), and absorption (c, f) spectra for TM (a-c) and TE (d-f) incident white light and θ_i= 30° with change of cavity depth h_1. The other simulation parameters are same with that in Fig. 2.

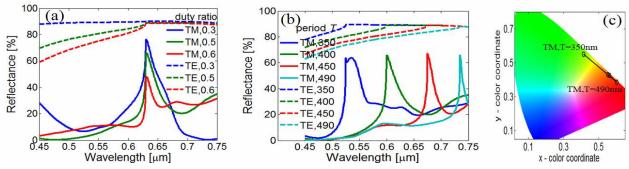

Fig. 6. Simulated TM (solid lines) and TE (dashed lines) reflection for h_1= *90 nm and* θ_i= 30° with change of duty ratio (a) and grating pitch T (b). (c) The locations in the CIE 1931 xy chromaticity diagram for TM reflected spectra in (b). The other simulation parameters are same with that in Fig. 2.

4. Conclusion

In summary, we have proposed a metallic/dielectric hybrid grating structure to achieve reflective low-side-band plasmonic structural colors. The device demonstrates narrow and high monochromatic-peaked reflection for TM white light which renders bright and vivid colors. Three physical mechanisms are responsible for these features, including SPR enhanced reflection, remarkable diffraction of light at shorter wavelengths, strong absorption by metal-surrounding nano-cavities and silicon substrates for the light at longer wavelengths beyond diffraction. Without these mechanisms, TE light shows wide band reflection. It may find wide applications, for example, producing novel reflective anti-counterfeit films. Normally, the color shift by the anti-counterfeit film is produced by the grating diffraction effects. Here with our structure, besides the diffraction, reflected colors changing obviously with the incident angle and polarization make the anti-counterfeit film more conspicuous.

Acknowledgments

The authors acknowledge the support of National Natural Science Foundation of China (Grant Nos. 61370047, 11374212, 61007025, 51235007, and 11421064).